



**HAL**  
open science

## Modulation of equatorial turbulence by tropical instability waves

Ren-Chieh Lien, Eric A. d'Asaro, Christophe E. Menkès

► **To cite this version:**

Ren-Chieh Lien, Eric A. d'Asaro, Christophe E. Menkès. Modulation of equatorial turbulence by tropical instability waves. *Geophysical Research Letters*, 2008, 35, pp.24607. 10.1029/2008GL035860 . hal-00770554

**HAL Id: hal-00770554**

**<https://hal.science/hal-00770554>**

Submitted on 29 Oct 2021

**HAL** is a multi-disciplinary open access archive for the deposit and dissemination of scientific research documents, whether they are published or not. The documents may come from teaching and research institutions in France or abroad, or from public or private research centers.

L'archive ouverte pluridisciplinaire **HAL**, est destinée au dépôt et à la diffusion de documents scientifiques de niveau recherche, publiés ou non, émanant des établissements d'enseignement et de recherche français ou étrangers, des laboratoires publics ou privés.

Copyright

## Modulation of equatorial turbulence by tropical instability waves

Ren-Chieh Lien,<sup>1</sup> Eric A. D'Asaro,<sup>1</sup> and Christophe E. Menkes<sup>2</sup>

Received 29 August 2008; accepted 16 October 2008; published 24 December 2008.

[1] The sea surface temperature in the Pacific equatorial cold tongue is influenced strongly by the turbulent entrainment flux. A numerical model using a level-1.5 turbulence closure scheme suggests strong modulation of the entrainment flux by tropical instability waves (TIWs). Turbulence observations taken by a Lagrangian float encountering a TIW confirm the spatial pattern of turbulent flux variation predicted by the model. The strongest observed turbulence mixing occurred at the leading edge of the TIW trough; turbulence diffusivity  $K \sim 10^{-2} \text{ m}^2 \text{ s}^{-1}$  and turbulent heat flux  $Q \sim 1000 \text{ W m}^{-2}$  at the base of surface mixed layer. The weakest observed turbulence occurred at  $\sim 2^\circ$  south of the TIW trough;  $K \sim 10^{-4} \text{ m}^2 \text{ s}^{-1}$  and  $Q \sim 10 \text{ W m}^{-2}$ . The TIW caused nearly two decades of turbulence variation within an  $O(1000 \text{ km})$  zonal scale and  $O(100 \text{ km})$  meridional scale. Model results suggest that the increased entrainment heat flux at the leading edge of the TIW trough can be explained by the enhancement of shear at the surface mixed layer base modulated by the TIWs. **Citation:** Lien, R.-C., E. A. D'Asaro, and C. E. Menkes (2008), Modulation of equatorial turbulence by tropical instability waves, *Geophys. Res. Lett.*, *35*, L24607, doi:10.1029/2008GL035860.

### 1. Introduction

[2] The equatorial cold tongue is a conduit with continuous mass and heat exchanges: upwelling brings cold water to near the surface, turbulence entrainment flux brings it into the cold tongue and the surface Ekman divergence then exports it from the cold tongue poleward, while zonal and meridional eddy advection and atmospheric fluxes warm the cold tongue [Kessler *et al.*, 1998; Swenson and Hansen, 1999; Menkes *et al.*, 2006].

[3] Microstructure measurements taken within the cold tongue at equator  $140^\circ\text{W}$  in 1984, 1987, and 1991 reveal the unique nighttime enhancement of turbulence not only in the surface mixed layer, but several tens of meters below the base of surface mixed layer within a strongly shear stratified layer, referred to as the deep-cycle layer [Gregg *et al.*, 1985; Moum and Caldwell, 1985; Peters *et al.*, 1988; Lien *et al.*, 1995]. Turbulent heat fluxes at the base of the surface mixed layer estimated from microstructure measurements show a wide range of variations,  $10\text{--}100 \text{ W m}^{-2}$ . Wang and McPhaden [1999, 2001] computed all terms in the heat budget equation directly from mooring data, except the entrainment flux, which was estimated as the residual of

the heat balance. They found that the primary balance in the central and eastern equatorial Pacific is between cooling by the turbulent heat flux at the base of the surface mixed layer ( $\sim 100 \text{ W m}^{-2}$ ) and warming by the atmosphere and by the meridional heat fluxes ( $\sim 50 \text{ W m}^{-2}$  each). Of all these processes, the turbulent entrainment heat flux is the least understood and is the focus of this study.

[4] Tropical instability waves (TIWs) are prominent features in the central and eastern equatorial Pacific, propagating westward at  $0.3\text{--}0.5 \text{ m s}^{-1}$  with a period of 15–40 days and a wavelength of  $\sim 700\text{--}1600 \text{ km}$  [Lyman *et al.*, 2007]. Previous space-borne sea surface temperature (SST) measurements, in-situ measurements, and numerical models reveal strong modulations of the equatorial current, thermal structures, and the air–sea fluxes by TIWs [Chelton *et al.*, 2000; Kennan and Flament, 2000; Vialard *et al.*, 2003; Menkes *et al.*, 2006]. Recent numerical model results suggest that the turbulence mixing is also modulated by TIWs [Menkes *et al.*, 2006; Dutrieux *et al.*, 2008]. Here, we present the first observations of strong modulation of turbulent diffusivities and heat fluxes by TIWs. The observed spatial pattern supports the numerical model results.

### 2. Lagrangian Float

[5] Within the equatorial cold tongue, the vertical turbulent heat flux  $Q(z)$  is negative in the surface mixed layer, bringing cold water upward. It acts to cool the boundary layer balancing the warming from the atmosphere and from horizontal heat flux divergences. In the surface mixed layer, the vertical flux divergence  $\partial_z Q$  is positive and  $Q$  increases in magnitude with depth. Below the surface mixed layer and within the deep-cycle turbulence layer, the magnitude of  $Q$  decreases, vanishing at the base of the deep-cycle layer [Gregg *et al.*, 1985; Moum and Caldwell, 1985]. The maximum magnitude of  $Q$  exists at the base of the surface mixed layer.

[6] In this study, the turbulent heat flux was measured by a Lagrangian float placed immediately below the base of the surface mixed layer near this heat flux maximum. Each day the float profiled from the sea surface to about 130-m depth and, based on the potential density measured on this profile, chose a target potential density surface  $0.1 \text{ kg m}^{-3}$  greater than the surface mixed layer potential density. The float then adjusted its potential density to this target and settled onto the target isopycnal surface for the rest of the day (Figure 1c).

[7] The float (Figure 1a) was deployed on September 8, 2005 at the equator and  $125^\circ\text{W}$ . During its isopycnal drifts it measured pressure at the center of the float, temperature and conductivity at the bottom of the float, and temperature at the top of the float. The hull of the float is 1 m long and the vertical separation of temperature sensors at the two ends of

<sup>1</sup>Applied Physics Laboratory, University of Washington, Seattle, Washington, USA.

<sup>2</sup>LOCEAN, Institut de Recherche pour le Développement, Nouméa, New Caledonia.

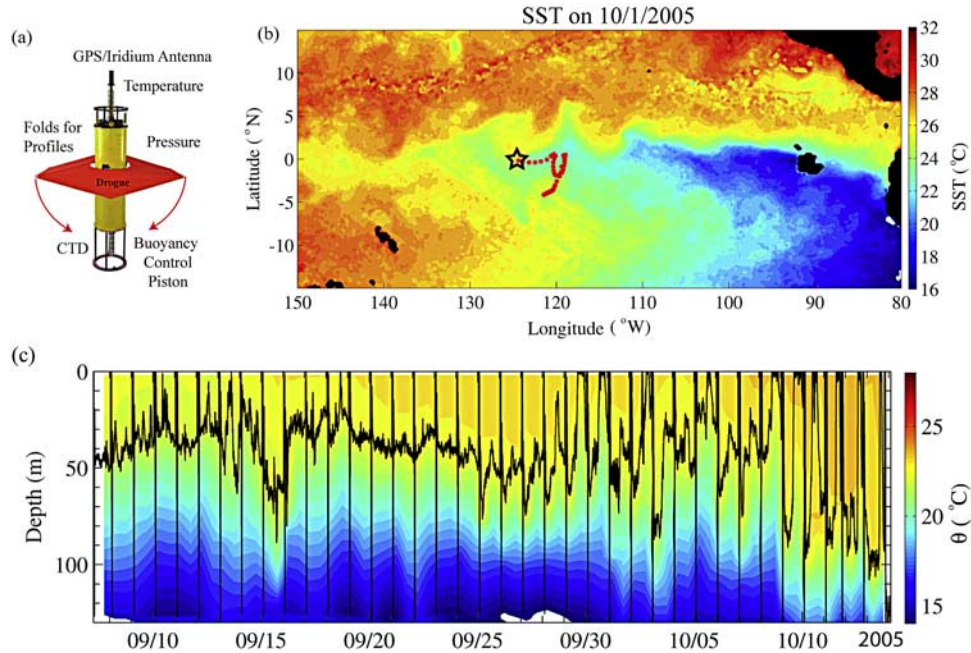


**Figure 1.** (a) Lagrangian float and sensors, (b) sea surface temperature on October 1, 2005 obtained from TMI, and the float trajectory between September 8 and October 10 (red dots), and (c) temperature (colors) along the Lagrangian float trajectory and the float's vertical trajectory (black line). The Lagrangian float was deployed on September 8, 2005 at equator  $125^{\circ}\text{W}$ , marked as the star in Figure 1b.

the float is 1.4 m. Pressure was sampled every 15 s and temperature and conductivity every 30 s. During profiles, the sampling interval varied from 5 to 30 s, resulting in profile data spacing from less than one to several meters. At the top of each profile the float obtained a GPS position, transmitted data via Iridium, and received the incoming mission commands. Problems with data transmission resulted in data at several temporal resolutions: high resolution (15 s), intermediate resolution (30 s), and low resolution (150 s). We received nearly 100% of the low-resolution data, and about 50% of the combined intermediate- and high-resolution data.

[8] Although the float was deployed at the equator, it was advected from this position by the ocean currents. Its meridional motion mostly reflects the currents from a passing TIW, moving to  $2^{\circ}\text{S}$  from September 15 to 25 and then back to the equator from September 25 to October 2, displaying a U-shaped trajectory (Figure 1b).

[9] Our equatorial float deployments, of which this is just one, have suffered from a peculiar and often severe degradation due to ocean biology. This is manifested as a diel variation in float buoyancy, with the float becoming heavier at sunset and lighter at sunrise. A small camera attached to the float on a later mission showed an associated diel variation in the presence of small fish around the float, suggesting that these are responsible for the problem. This effect typically became noticeable about one week after deployment and grew exponentially in time, sometimes terminating the float mission and sometimes abruptly disappearing. The large buoyancy changes, sometimes exceeding 100 g, made it difficult to control the float's buoyancy and thus depth. For the float described here, the daytime buoyancy increases caused frequent surfacing after Septem-

ber 30 (Figure 1c). After October 6, the effect became severe and the data were excluded from the present analysis.

### 3. Turbulence Measurements

[10] Two independent methods were used to estimate the turbulent buoyancy flux  $J$  from Lagrangian float measurements. First, the dissipation rate of turbulence kinetic energy  $\varepsilon$  was estimated using an inertial subrange method [Lien and D'Asaro, 2006] and a mixing efficiency of  $\Gamma = 0.2$  yielding  $J_{\varepsilon} = \Gamma\varepsilon$  [Osborn, 1980]. Second, flux was computed using direct covariance  $J_C = \langle w'b' \rangle$ , where  $w'$  is the perturbation vertical velocity and  $b' = g\rho'/\rho_0$  is the perturbation buoyancy. For each estimate of  $J_{\varepsilon}$  and  $J_C$  a diffusivity  $K = J/N^2$  is computed, where  $N$  is the buoyancy frequency, yielding estimates  $K_{\varepsilon}$  and  $K_C$ . The buoyancy frequency  $N$  is computed using density estimated at the two ends of the float; the salinity at the top of the float is not measured and is assumed to be the same as that measured at the bottom of the float.

[11] Problems exist with both methods. However, because the two methods are independent and subject to different errors, their good agreement gives confidence in our overall analysis (Figure 2a). The final estimate of diffusivity  $K$  (thick grey line in Figure 2a) is made using whichever method is available at a given time in the observation period and the average of both when they are available. The turbulent heat flux is computed as  $Q = \rho C_p K \partial_z \theta$ , where  $\rho C_p$  is the specific heat of water per unit volume, and  $\partial_z \theta$  is the vertical gradient of temperature.

[12] The inertial subrange method for estimating  $\varepsilon$  from Lagrangian float data is described by Lien and D'Asaro [2006]. It is found to agree with the standard '-5/3'

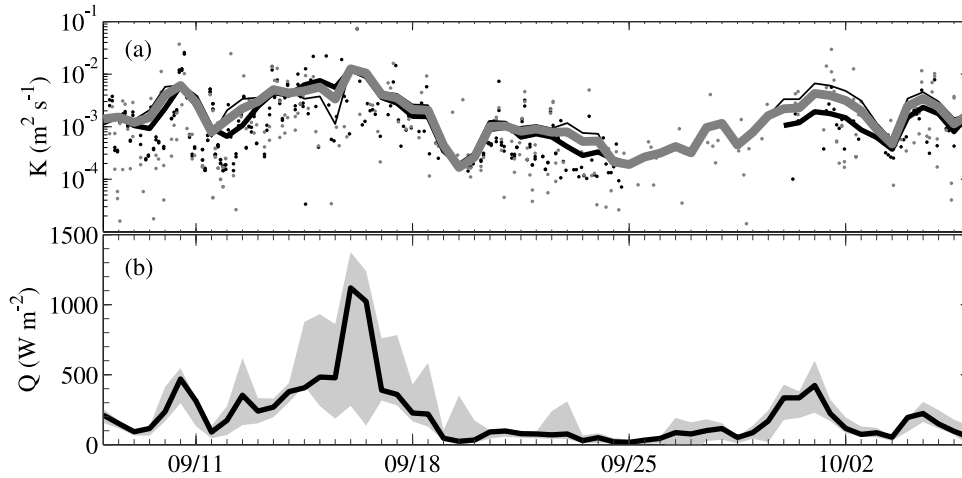


**Figure 2.** Time series of (a) estimates of turbulence diffusivity  $K_\varepsilon$  (thick black curve),  $K_C$  (thin black curve), and their average (thick grey curve). Dots show 2-hr averages; curves show 12-hr averages. (b) Estimates of turbulent heat flux. Shading shows the 95% confidence interval of the mean turbulent heat flux.

Eulerian inertial subrange method to better than a factor of 2 for  $\varepsilon$  from  $10^{-8}$  to  $10^{-4}$   $\text{W kg}^{-1}$ . The method relies on the existence of a Lagrangian inertial subrange, similar to the ‘ $-5/3$ ’ inertial subrange in the wavenumber spectrum. Kolmogorov scaling predicts that the vertical acceleration spectrum  $\Phi_a$  is white, i.e.,  $\Phi_a(\omega) = \beta\varepsilon$ , where the Kolmogorov constant  $\beta = 1.9 \pm 0.1$  is determined from previous numerical models, and laboratory and field observations [Lien and D’Asaro, 2002]. In reality, the spectrum has a more complex form, limited at low frequencies by the largest turbulent eddies with a frequency  $\omega_0$ , and at high frequencies by the finite size of the float and the pressure sensor noise. Lien *et al.* [1998] report a general form of this spectrum  $\tilde{\Phi}_a(\omega; \omega_0, \varepsilon)$ . The value of  $\varepsilon$  is found by fitting this form to the measured spectra computed in 2-hr segments. Because the inertial subrange method requires relatively high-frequency data, only segments with intermediate- and high-resolution sampling could be used.

[13] The covariance flux  $J_C$  was computed directly from the perturbation vertical velocity and buoyancy defined by a high-pass Butterworth filter with the half power point at 1800 s, more than twice the typical buoyancy period. Estimates of  $J_C$  were computed every 2 hr. Because the covariance flux is dominated by eddies near  $N$ , data with all temporal resolutions could be used.

[14] Figure 2a shows the 2-hr estimates of  $K_\varepsilon$  and  $K_C$  (dots) and their 12-hr averages (curves). The 12-hr averaged turbulent heat flux  $Q$  shows nearly two decades of variation, from  $\sim 10$   $\text{W m}^{-2}$  on September 19 and 25 to  $1100$   $\text{W m}^{-2}$  on September 16 (Figure 2b). In the next section, we show that this observed two decades of variation in turbulent heat flux is correlated with the phase of a passing TIW.

#### 4. Effects of TIWs on Equatorial Turbulence Mixing

[15] The large variations in entrainment heat flux occurred as a TIW front passed north of the float. The westward speed of the TIW was estimated at  $\sim 0.42$   $\text{m s}^{-1}$  by comparing daily  $24^\circ\text{C}$  SST fronts observed by the TRMM (Tropical Rainfall Measuring Mission) Microwave

Imager (TMI). Figure 3a shows the TIW structure and float trajectory in a coordinate system moving with the wave. The average  $24^\circ\text{C}$  front (Figure 3a, red curve) is displaced northward during the ‘‘cold phase’’ of the TIW and southward during the ‘‘warm phase.’’ The values of  $K$  and  $Q$  (red curves in Figures 3b and 3d) vary coherently with the wave phase.

[16] Menkes *et al.* [2006] employ a numerical model to study the climatological heat budget associated with TIWs. The model is forced by climatological heat and water forcing and interannual seven-day ERS  $1^\circ$  lat.  $\times$   $1^\circ$  lon. stress over the 1993–1996 period. Horizontal grid spacing is  $1^\circ$  lon.  $\times$   $0.5^\circ$  lat. The vertical turbulent mixing is parameterized using a level-1.5 turbulence closure scheme, with a prognostic equation for turbulence kinetic energy and a diagnostic equation for turbulence length scale [Blanke and Delecluse, 1993]. The model  $K$  and  $Q$  also exhibit a strong modulation by TIWs (color contours in Figures 3a and 3c).

[17] The model forcing and background conditions are different from those during our float observations. The model TIW has a zonal scale 20% longer than that during float observations and the model temperature is somewhat warmer than that observed. Nonetheless, the variation in the model’s  $25.5^\circ\text{C}$  isotherm (black curves in Figures 3a and 3c), after adjusting the wavelength, agrees well with the observed variation in the  $24^\circ\text{C}$  isotherm (red curves in Figures 3a and 3c).

[18] Because the differences between observed and model TIWs and differences in the observed and model background oceanic conditions and surface forcing, we do not expect good agreement between model and observed absolute values of turbulent heat fluxes. Here, we focus on the comparison of the spatial pattern of turbulent entrainment flux with TIW phase. The model predictions of  $K$  and  $Q$  along the float track agree well with the observations, in phase of the TIW, with the strongest mixing occurring at the transition from cold to warm phase, but are somewhat weaker in amplitude (compare red and black curves in Figures 3b and 3d, and colored circles in Figures 3a and 3c).

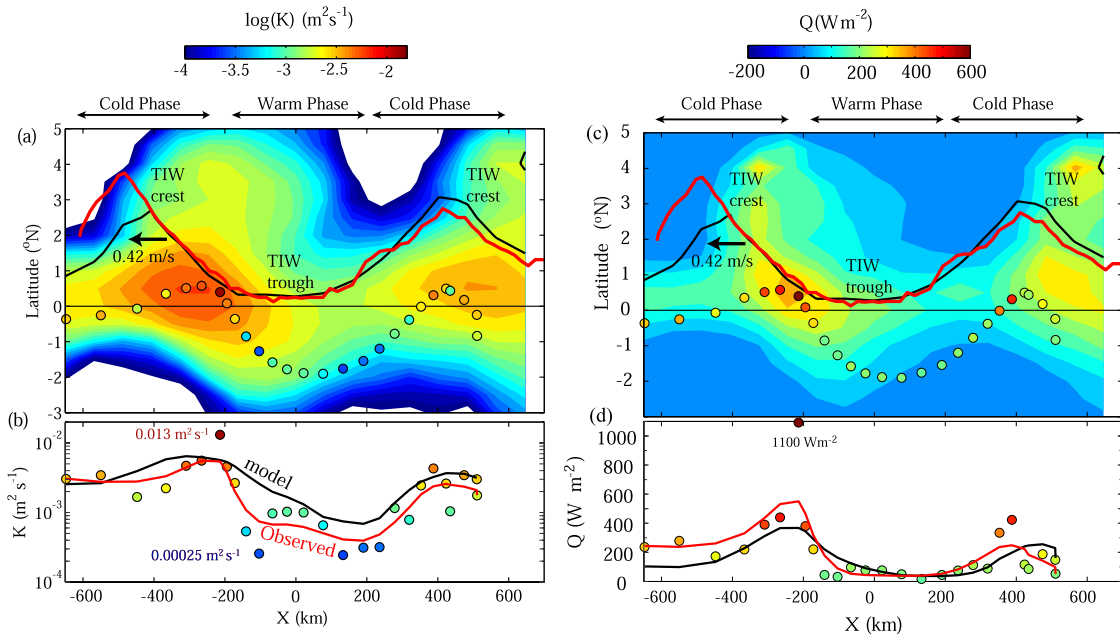


**Figure 3.** (a) Turbulent diffusivity at the mixed layer base estimated from Lagrangian float measurements (filled colored circles) along the float trajectory and from the model (color contour) [Menkes *et al.*, 2006]. The red curve is the  $24^\circ\text{C}$  SST isotherm observed between September 10 and October 6, 2005. The black curve is the  $25.5^\circ\text{C}$  isotherm from the model. (b) The observed turbulence diffusivity (filled colored circles) compared with the model results along the float trajectory (black curve). The red curve is the low-pass filtered observed turbulence diffusivity. Two extreme values of turbulence diffusivity are labeled. The warm and cold phases of TIWs are referred to by their SST signature and are labeled crudely for convenience to illustrate the turbulence variations with respect to TIWs. (c and d) Symbols same as in Figures 3a and 3b but for entrainment heat flux at the mixed layer base.

[19] The strong modulation of turbulent entrainment heat flux corresponds to the similar variation of  $K$  at the TIW scale (Figures 3a and 3c). We revisit the turbulence closure scheme used in the model [Menkes *et al.*, 2006] to understand the dynamics of this modulation. The vertical eddy diffusivity is proportional to the product of the squared root of turbulent kinetic energy ( $e$ ) and a diagnostic turbulence length scale ( $\ell$ ), which in a stably stratified region with constant  $N$  is given by  $\ell \propto e^{1/2} N^{-1}$ . The prognostic equation for  $e$ , ignoring the transport terms, may be expressed as

$$\frac{de}{dt} \approx CeN^{-1} [S^2 - \alpha N^2] = CeN^{-1} S_{red}^{*2},$$

where  $C \sim 0.1$  is a constant,  $\alpha = 4.38$  for  $Ri = N^2/S^2 > 0.2$  and  $\alpha = 4.5$  for  $Ri \leq 0.2$ . The model reduced shear squared  $S_{red}^{*2} = (S^2 - \alpha N^2)$  is similar to the reduced shear squared  $S_{red}^2 = (S^2 - 4N^2)$  used in the turbulence parameterization scheme for shear instability suggested by Kunze *et al.* [1990]. In the model, the turbulent kinetic energy  $e$ , and thus the diffusivity, increases when the model reduced shear squared  $S_{red}^{*2} > 0$  and decreases when  $S_{red}^{*2} < 0$ . Figure 4 shows the strong modulation of model  $S_{red}^{*2}$  at the base of the surface mixed layer with a pattern similar to that of variation of entrainment heat flux; positive  $S_{red}^{*2}$  occurs mostly in the cold phase of TIW. Model results of  $S_{red}^{*2}$  exhibit a similar pattern. Therefore, the variations in the turbulent entrain-

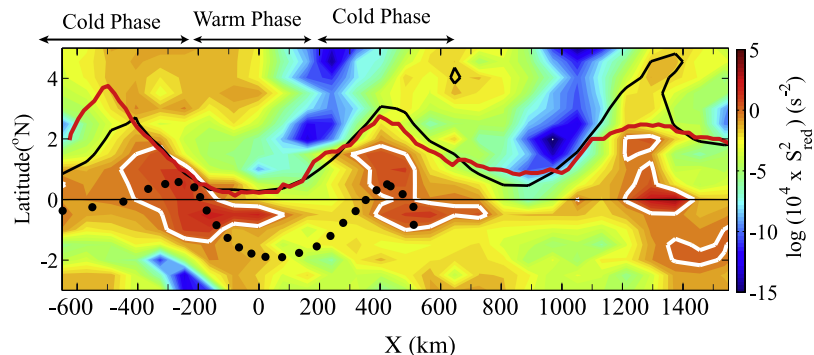


**Figure 4.** Model results of reduced shear squared ( $S^2 - 4N^2$ ) at the base of the surface mixed layer. The red curve is the  $24^\circ\text{C}$  SST isotherm observed between September 10 and October 6, 2005. The black curve is the  $25.5^\circ\text{C}$  isotherm from the model. Black dots represent float trajectory. White lines delineate contours of zero reduced shear squared.

ment flux in the model can be explained by the variations in the reduced shear squared at the mixed layer base modulated by the TIWs. We have also tested a simple wind-driven model of the entrainment flux with  $\varepsilon_{wind} = u_*^3 / \kappa z$ , where  $u_*$  is friction velocity [Charnock, 1955] computed from the TMI wind product,  $\kappa = 0.4$  von Karman constant, and  $z$  is the float depth, and found that this model cannot explain either the overall magnitude or the fluctuation phase of the entrainment flux (not shown).

## 5. Summary

[20] A Lagrangian float measured turbulent entrainment flux below the equatorial cold tongue during the passage of a TIW. Turbulence mixing was modulated strongly by the TIW. Turbulence was the strongest at the leading edge of the TIW trough, the transition from the cold to the warm phases of the TIW, with a maximum  $K$  of  $0.013 \text{ m}^2 \text{ s}^{-1}$ , maximum  $Q$  of  $1100 \text{ W m}^{-2}$ , and maximum  $\varepsilon$  of  $3 \times 10^{-6} \text{ W kg}^{-1}$ . Turbulence was the weakest when the float was displaced to  $2^\circ\text{S}$  by the TIW, where  $K = O(10^{-4} \text{ m}^2 \text{ s}^{-1})$ ,  $Q \sim 10 \text{ W m}^{-2}$ , and  $\varepsilon = O(10^{-7} \text{ W kg}^{-1})$ . The observed spatial pattern of the entrainment heat flux at TIW scale supports results from a recent numerical model [Menkes *et al.*, 2006]. Further investigation of model results suggests that the modulation of the entrainment heat flux at TIW scale can be explained by the variations in reduced shear at the mixed layer base induced by the TIW.

[21] The turbulent heat flux below the equatorial cold tongue is the major factor in cooling the surface of the eastern equatorial Pacific. Variations in this flux during the El Niño/La Niña cycle play a key role in the dynamics of ENSO. Predictive models of ENSO evolution need to properly include the modulation effects of TIW on turbulent heat flux. Our observations suggest that accurate modeling of these effects is possible.

[22] **Acknowledgments.** This work was funded by the National Science Foundation grant 0241244. We are grateful to the engineering group at the Applied Physics Laboratory and to the Tropical Atmosphere Ocean project office at Pacific Marine Environmental Laboratory in Seattle, especially to the mooring group, for their help with Lagrangian float deployments. Christophe Menkes thanks IRD for support and IDRIS for calculation time.

## References

Blanke, B., and P. Delecluse (1993), Variability of the tropical Atlantic Ocean simulated by a general circulation model with two different mixed layer physics, *J. Phys. Oceanogr.*, *23*, 1363–1388.  
 Charnock, H. (1955), Wind stress on a water surface, *Q. J. R. Meteorol. Soc.*, *81*, 639–640.

Chelton, D. B., F. J. Wentz, C. L. Gentemann, R. A. de Szoeke, and M. G. Schlax (2000), Satellite microwave SST observations of transequatorial tropical instability waves, *Geophys. Res. Lett.*, *27*, 1239–1242.  
 Dutrieux, P., C. Menkes, J. Vialard, P. Flament, and B. Blanke (2008), Lagrangian study of tropical instability vortices in the Atlantic, *J. Phys. Oceanogr.*, *38*, 400–417.  
 Gregg, M. C., H. Peters, J. C. Wesson, N. S. Oakey, and T. J. Shay (1985), Intensive measurements of mixing of turbulence and shear in the equatorial undercurrent, *Nature*, *318*, 140–144.  
 Kennan, S. C., and P. Flament (2000), Observations of a tropical instability vortex, *J. Phys. Oceanogr.*, *30*, 2277–2301.  
 Kessler, W. S., L. M. Rothstein, and D. Chen (1998), The annual cycle of SST in the eastern tropical Pacific, diagnosed in an ocean GCM, *J. Clim.*, *11*, 777–799.  
 Kunze, E., M. G. Briscoe, and A. J. Williams III (1990), Interpreting shear and strain fine structure from a neutrally buoyant float, *J. Geophys. Res.*, *95*, 18,111–18,125.  
 Lien, R.-C., and E. A. D’Asaro (2002), The Kolmogorov constant for the Lagrangian velocity spectrum and structure function, *Phys. Fluids*, *14*, 4456–4459.  
 Lien, R.-C., and E. A. D’Asaro (2006), Measuring dissipation rates of turbulence kinetic energy with a Lagrangian float, *J. Atmos. Oceanic Technol.*, *23*, 964–976.  
 Lien, R.-C., D. R. Caldwell, M. C. Gregg, and J. N. Moum (1995), Turbulence variability at the equator in the central Pacific at the beginning of the 1991–1993 El Niño, *J. Geophys. Res.*, *100*, 6881–6898.  
 Lien, R.-C., E. A. D’Asaro, and G. Dairiki (1998), Lagrangian frequency spectra of vertical velocity and vorticity in high-Reynolds-number oceanic turbulence, *J. Fluid Mech.*, *362*, 177–198.  
 Lyman, J. M., G. C. Johnson, and W. S. Kessler (2007), Distinct 17- and 33-day tropical instability waves in subsurface observations, *J. Phys. Oceanogr.*, *37*, 855–872.  
 Menkes, C. E. R., J. G. Vialard, S. C. Kennan, J.-P. Boulanger, and G. V. Madec (2006), A modeling study of the impact of tropical instability waves on the heat budget of the eastern equatorial Pacific, *J. Phys. Oceanogr.*, *36*, 847–865.  
 Moum, J. N., and D. R. Caldwell (1985), Local influences on the shear-flow turbulence in the equatorial ocean, *Science*, *230*, 315–316.  
 Osborn, T. R. (1980), Estimates of the local rate of vertical diffusion from dissipation measurements, *J. Phys. Oceanogr.*, *10*, 83–89.  
 Peters, H., M. C. Gregg, and J. M. Toole (1988), On the parameterization of equatorial turbulence, *J. Geophys. Res.*, *93*, 1199–1218.  
 Swenson, M. S., and D. V. Hansen (1999), Tropical Pacific ocean mixed layer heat budget: The Pacific cold tongue, *J. Phys. Oceanogr.*, *29*, 83–91.  
 Vialard, J., C. Menkes, D. L. T. Anderson, and M. Balsameda (2003), Sensitivity of Pacific Ocean tropical instability waves to initial conditions, *J. Phys. Oceanogr.*, *33*, 105–121.  
 Wang, W., and M. J. McPhaden (1999), The surface-layer heat balance in the equatorial Pacific. Part I: Mean seasonal cycle, *J. Phys. Oceanogr.*, *29*, 1812–1831.  
 Wang, W., and M. J. McPhaden (2001), Surface layer temperature balance in the equatorial Pacific during the 1997–1998 El Niño and the 1998–1999 La Niña, *J. Clim.*, *14*, 3393–3407.

E. A. D’Asaro and R.-C. Lien, Applied Physics Laboratory, University of Washington, 1013 NE 40th Street, Seattle, WA 98105, USA. (lien@apl.washington.edu)

C. E. Menkes, LOCEAN, Institut de Recherche pour le Développement, BP A5, 98848 Nouméa CEDEX, New Caledonia.